



Short communication

Influence of Zn^{2+} in $CoFe_2O_4$ nanoparticles on its photocatalytic activity under solar light irradiation

Revathi J^a, John Abel M^b, Lydia Pearline C^c, Sumithra T^b, Fermi Hilbert Inbaraj P^b, Joseph prince J^{b,*}

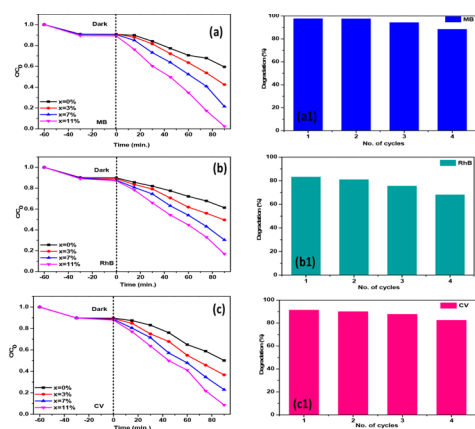
^a Department of Physics, St. Antony's College of Arts and Sciences for Women, Ammakulathupatti, Tamil Nadu 624005, India

^b Department of Physics, University College of Engineering, Bharathidasan Institute of Technology Campus, Anna University, Tiruchirappalli 24, Tamil Nadu, India

^c Department of Electronics and Communication Engineering, University College of Engineering, Bharathidasan Institute of Technology Campus, Anna University, Tiruchirappalli 620 024, Tamil Nadu, India



GRAPHICAL ABSTRACT



ARTICLE INFO

Keywords:

Sunlight irradiation
Spinel ferrites
Photocatalytic activity
Textile dyes
Optical properties

ABSTRACT

The present work deals with the study of $CoFe_2O_4$ and three different concentrations of Zn^{2+} substituted $CoFe_2O_4$ nanoparticles synthesized via a simple co-precipitation method as a sunlight driven photocatalyst. Powder X-ray diffraction studies were taken to preliminary confirmation of crystal structure and crystallite size were found to be 43 nm, 41 nm, 40 nm, and 37 nm for $Zn_xCo_{(100-x)}Fe_2O_4$ ($x = 3$ wt%, 7 wt%, 11 wt%) samples respectively. optical band gap was found to be 1.85 eV, 1.99 eV, 2.08 eV and 2.28 eV $Zn_xCo_{(100-x)}Fe_2O_4$ ($x = 3$ wt%, 7 wt%, 11 wt%) samples respectively using diffused reflectance spectroscopy (UV-DRS). The Photoluminescence (PL) study was carried out for crystal defect analysis. Fourier transforms infrared (FTIR) spectroscopy gives the details about the functional group present in the material. Scanning electron microscopy and energy dispersive X-ray spectrum (SEM & EDAX) show the surface morphology and elemental composition of the synthesized material. Rhodamine B (RhB), Methylene Blue (MB) and Crystal Violet (CV) are mineralized by photodegradation using synthesized material was studied.

* Corresponding author.

E-mail address: josephprinceaut@gmail.com (J. Joseph prince).

<https://doi.org/10.1016/j.inoche.2020.108186>

Received 24 June 2020; Received in revised form 15 August 2020; Accepted 15 August 2020

Available online 19 August 2020

1387-7003/ © 2020 Elsevier B.V. All rights reserved.

1. Introduction:

Investigating the materials at their nano-scale dimensions gets intensive attention by researchers due to their high surface to volume ratio which results in enhanced properties of those materials in comparison with the bulk counterparts. The process of photocatalytic degradation with the help of semiconductor compounds like TiO_2 and ZnO , which is also one of the green chemistry technologies was paid much attention during the past two decades, for the remediation of polluted groundwater and hazardous debris [1,2]. Besides these, the visible-light-active photocatalysts have a considerable attracting interest because of their high competence in the utilization of the solar spectrum. Although ZnO and TiO_2 , exhibit better photocatalytic activity under UV light irradiation, it shows poor performance under visible spectrum owing to their relatively huge band gap energy of about 3.2 eV. Many alterations were carried out to broaden the absorption wavelength range of these UV-active metal oxides into the visible range [3,4]. Other visible-light active photocatalysts, such as Fe_2O_3 , CdS and WO_3 are developed to extend the absorption wavelength range to the visible region; but their low photocatalytic activities and low stabilities limit its practical application [5–7]. In this regard, the development of visible-light active photocatalysts has always been a hot issue in recent decades. Now a day, spinel metal oxide (AB_2O_4) has greater attention and utilized for many applications such as gas sensors supercapacitors, hydrogen storage, photo-diodes, solar cells, battery anode material, etc. because of their cationic distributions along the surfaces [8–13]. In the normal spinel structure, A is divalent cations occupy one-eighths of tetrahedral voids and B is trivalent cations that take up half of the octahedral sites, and these atoms are distributed into FCC lattice constituted by the ligand O^{2-} ions [14]. Mixed spinel or inverse spinel structure [B (AB) O_4], may modify their crystal structure in such a way that trivalent cations occupy both the octahedral sites and tetrahedral sites whereas divalent cations occupy octahedral sites [15]. Researchers now focused on these spinel nano-crystals for the photocatalytic remediation of wastewater treatments owing to their cationic distributions. For instance, Youcun Chen et al. developed Co_3O_4 for degrading methyl orange dye in aqueous solution [16]. CuAl_2O_4 was fabricated by Hassanzadeh-Tabrizi et al. and photocatalytic activity was carried out on methyl orange [17]. Rhodamine B (RhB) and Methylene Blue (MB) dye were degraded using NiMn_2O_4 thin-films are reported by Larbi et al. [18]. The studies on photocatalytic activity of spinel aluminate (Mg, Cu, Zn: Al_2O_4) was reported by Jiang et al. using three different dyes such as methyl orange, reactive brilliant red and acid red B [19]. On the other hand the ferrite based spinel materials having the general formula of A: Fe_2O_4 (A = Mg, Mn, Zn, Ni, and Co) are synthesized due to their remarkable magnetic, electrical, and optical properties [20–22]. Also spinel ferrites were utilized for the photocatalytic activity for their reusable ability, chemical stability, broad absorption wavelength range, some literature is as follows. Photocatalytic activity of Aluminium doped Zinc Ferrite on Orange I dye has reported by A. I Borhan et al. [23]. M. Rahimi-Nasrabadi et al. has reported the photocatalytic activity of Ce doped Copper Ferrite using Methyl orange dye [24]. CuFe_2O_4 , CoFe_2O_4 , NiFe_2O_4 , and ZnFe_2O_4 were prepared by R. Sharma et al. and a comparative study on its photodegradation of Remazol Black 5 (RB5) was observed [25]. K. S. Jesudoss et al. studied the photodegradation efficiency of Mn-doped NiFe_2O_4 using Indigo carmine (IC) dye [26]. Besides this CoFe_2O_4 , is one of the spinel ferrites vastly used in various applications such as magnetic optical behavior, antibacterial, sensor, cancer treatment, electrical, biomedical, etc. [27–33]. CoFe_2O_4 was also utilized as photocatalysts for the mineralization of organic dyes. For example, $\text{CoFe}_2\text{O}_4/\text{AgBr}$ nanocomposite was fabricated by Zhenlu Li et al. observing the photocatalytic activity on Methyl orange, RhB and MB [34]. M. Sundararajan et al. reports Mg-doped CoFe_2O_4 NPs for degrading RhB dye. [35]. A. Kalam et al. report CoFe_2O_4 NPs degrading Methylene Blue (MB) [36]. Graphene assisted CoFe_2O_4 NPs for degrading MB dye was reported by L. Gan et al. [37].

This work deals with the study of Zn doped CoFe_2O_4 nanoparticles synthesized via a simple co-precipitation method for sunlight irradiated photocatalytic applications. Cobalt ferrite has lesser photocatalytic activity due to its small band gap energy whereas zinc oxide has good efficiency due to its large band gap value but only under UV light irradiation. This work aims to enhance the photocatalytic performance of cobalt ferrite by increasing its band gap using Zn^{2+} ions. Among the various methods of preparations of nanoparticles namely sol-gel, microwave-assisted, hydrothermal, fuel-combustion, ball milling, etc.; the chemical co-precipitation method is more attractive because of its simplest and easiest way of preparing metal oxide nanoparticles, the precursor preparation is simple, all the reaction parameters like temperature, pH, etc. were easy to control during the reaction itself, also control growth of crystallite size can be achieved easily and the yield was high. Further, the experimental observations of photocatalytic activity of as-prepared NPs were carried out using three different dyes namely Methylene Blue (MB), Crystal Violet (CV), and Rhodamine B (RhB) under direct sunlight irradiation.

2. Materials used for preparing CoFe_2O_4 and Zn-doped CoFe_2O_4 nanoparticles:

Merck brand chemicals and reagents with 99.9% purity are used for entire reactions without further purification. $\text{Co}(\text{NO}_3)_2 \cdot 6\text{H}_2\text{O}$ (Cobalt (II) nitrate hexahydrate), $\text{Fe}(\text{NO}_3)_3 \cdot 9\text{H}_2\text{O}$, (Ferric (III) nitrate nonahydrate), $\text{Zn}(\text{NO}_3)_2 \cdot 6\text{H}_2\text{O}$ (Zinc nitrate hexahydrate), are used as a precursor for cobalt, iron and zinc respectively. Sodium hydroxide pellets (NaOH), and double-distilled water are utilized as precipitating agent and solvent for the reaction respectively.

3. Synthesis procedure:

The pure CoFe_2O_4 and Zn-doped CoFe_2O_4 Nanoparticles (NPs) were synthesized by chemical co-precipitation method. Ferric precursor and cobalt precursor was taken in 2:1 ratio and dissolved one by one in 100 ml of distilled water with the help of a magnetic stirrer. A transparent homogenous mixture of two salts was obtained after a few minutes of constant and vigorous stirring. Then, 30 ml of (4 M) molarity, aqueous NaOH solution was taken in the burette and added slowly drop by drop into the homogenous mixture. After the complete addition of NaOH solution the mixture turns to light brown colour from transparent nature. The mixture was then allowed to a constant vigorous stirring for about 6hr. Then, the stirrer was stopped and the beaker containing reaction mixture is kept uninterrupted for a whole night so that the particles were completely settled at the bottom of the beaker as a precipitate. The precipitate is taken centrifuged three times each 20 min at 3000 rpm and washed with distilled and ethanol till the pH reaches neutral. Then the particle is spread over in the petri-dish and allowed to dry at 80 °C using a hot air oven. Finally, the particle was calcination for 2hr at 400 °C in a muffle furnace. The same procedure as mentioned above is followed step by step for the preparation of Zn-doped CoFe_2O_4 NPs by simply reducing the cobalt nitrate wt% and adding corresponding wt% of zinc nitrate to the reaction mixture. The samples $\text{Zn}_x \text{Co}_{(100-x)} \text{Fe}_2\text{O}_4$ (x = 3 wt%, 7 wt%, 11 wt%) are hereafter mentioned as CFO (pure CoFe_2O_4), ZCF1 (3% Zn), ZCF2 (7% Zn) and ZCF3 in the rest of the manuscript.

4. Photocatalytic experiment procedure:

Methylene Blue (MB), Crystal Violet (CV) and Rhodamine B (RhB) dyes are used as model organic contaminants. For the experimental analysis 5 mg/L dye solution of each dye and 100 ml in quantity was taken in separate beakers. 0.1 mg of the prepared photocatalysts and 2 ml of 30% solution hydrogen peroxide (H_2O_2) was used. A comparative analysis of photocatalyst in all compositions as prepared was examined separately. The sunlight is used as a photo source and all the

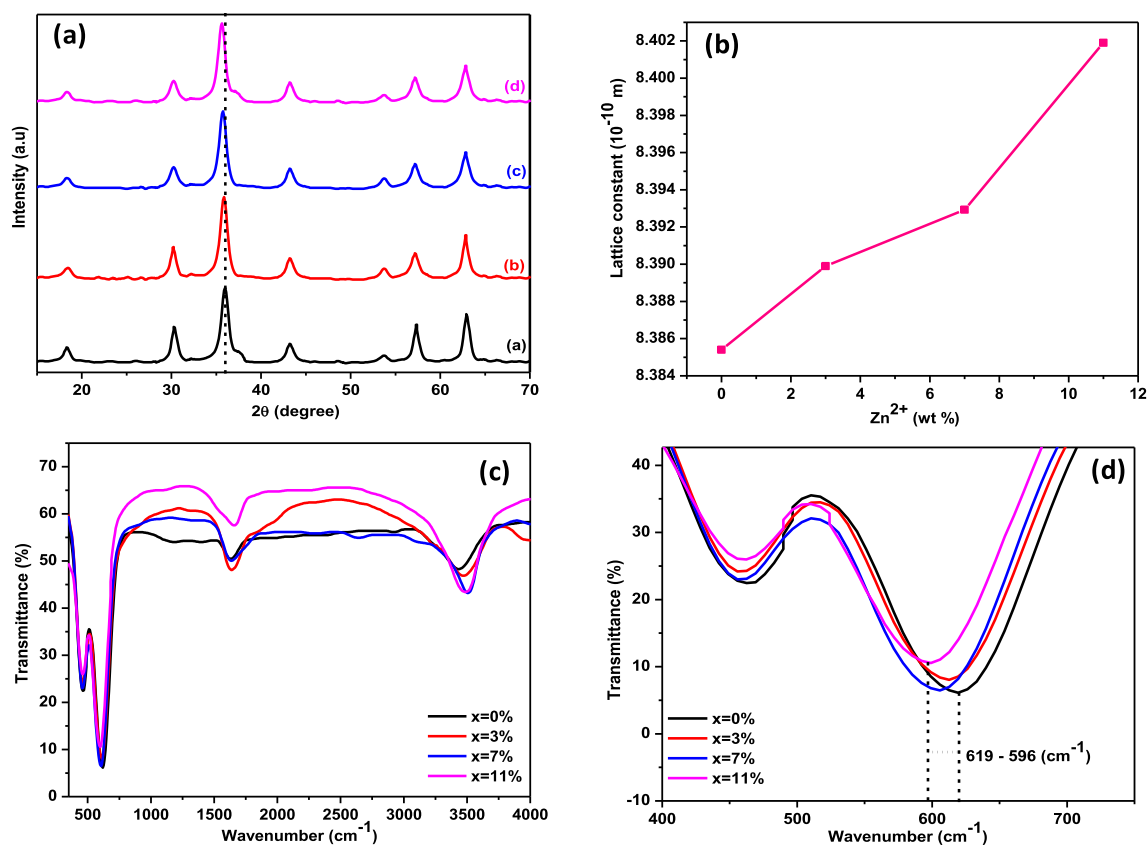


Fig. 1. (a) The powder X-ray diffraction pattern of CoFe₂O₄ and Zn-doped CoFe₂O₄ NPs, (b) graph between Zn wt % and lattice constant, (c & d) The FT-IR spectrum of CoFe₂O₄ and Zn-doped CoFe₂O₄ NPs.

dyes were taken in separate beakers. The stability of the as-prepared sample was also checked for four repeated cycles. The degradation percentage of the dye solution was calculated using the following formula.

$$\eta = \left(1 - \frac{c}{c_0}\right) \times 100 (\%) \quad (1)$$

5. Results and discussion

5.1. Powder X-ray diffraction (PXRD) studies

The PXRD study is a non-destructive study that is used to analyze the nature of the crystal structure, lattice parameters, phases and plane orientation of polycrystalline materials. The X-ray spectrum was recorded with 2θ ranges from 15 to 70°. The PXRD patterns of all the synthesized samples CFO, ZCF1, ZCF2 and ZCF3 are shown in Fig. 1a. The peaks were observed at respected 2θ values corresponding to the planes (1 1 1), (2 2 0), (3 1 1), (4 0 0), (4 4 0) and (5 1 1) are well-matched with the JCPDS No. 22-1012 and are suited with the scientific report reported by Singh et al. [38]. The most intense peak arose at 35.58° corresponding to the plane (3 1 1) confirms the cubic spinel structure of the prepared sample and belongs to the space group *Fd3m*. The lattice parameter was calculated using the following formula for the prepared samples.

$$a = d\sqrt{h^2 + k^2 + l^2} \quad (2)$$

There is an increase in the lattice parameter was observed from the calculated value with the increase in zinc content. Fig. 1b is the graph showing the dependence of the lattice parameter with respect to Zn²⁺ content. This linear increase in lattice constant (8.3854–8.4019 Å) is because of the replacement cobalt ion (0.78 Å) with the smaller ionic

radius when compared to zinc ions (0.84 Å) in the cobalt crystal lattice [39]. Similar variation in lattice constant values due to the incorporation of zinc cations was observed by Tatarchuk et al. [40]. Also the 2θ value of predominant peak is slightly shifted towards the lower angle side (35.79° – 35.58°) with the increased zinc content was observed, which may be due to the variation in lattice constant value. Using Scherrer formula the average crystallite size was calculated.

$$D = \frac{K\lambda}{\beta\cos\theta} \quad (3)$$

here (D) is the average crystallite size, K-shape factor, λ – incident X-ray wavelength (CuKα – 1.5406 Å), β- full width half maximum (FWHM), θ - diffraction angle. From the PXRD data the average crystallite size is calculated from the preferential plane (3 1 1) and is found to be 43 nm, 41 nm, 40 nm, and 37 nm for pure cobalt ferrite (CFO), 3 wt% Zn (ZCF1), 7 wt% Zn (ZCF2), and 11 wt% Zn (ZCF3)-doped samples respectively. The changes in the lattice parameter and the particle size with the Zn atom influence is narrated in Table 1..

5.2. FTIR analysis

The FTIR spectrum recorded in the frequency ranges of 350 – 4000 cm⁻¹ for CoFe₂O₄ and Zn-doped CoFe₂O₄ NPs is shown in Fig. 1c.

Table 1
XRD comparison table of CoFe₂O₄ and Zn-doped CoFe₂O₄ NPs.

Samples	Lattice parameter(Å)	Particle size (nm)
CFO	8.3854	43
ZCF1	8.3899	41
ZCF2	8.39293	40
ZCF3	8.4019	37

All the samples exhibit the absorption band at $\sim 1630\text{ cm}^{-1}$ and $\sim 3510\text{ cm}^{-1}$ is corresponding to H–O–H stretching and bending mode vibrations respectively [51]. The peak originates at $\sim 458\text{ cm}^{-1}$ (V_2) is associated with stretching vibration from tetrahedral sites and $619\text{--}596\text{ cm}^{-1}$ (V_1) is generally due to the stretching vibration from octahedral sites [52]. Thus the two M–O vibrations obtained from all the samples confirm the spinel crystal structure and is agree with the XRD results. Moreover, a slight shift towards the lower frequency was observed in the V_1 band ($619\text{--}596\text{ cm}^{-1}$) with the increase in Zn content as shown in Fig. 1d. This shift is maybe due to the occupancy of Zn^{2+} with larger ionic radii in the tetrahedral site and pushes the Fe^{3+} ions to the octahedral site [39].

5.3. Optical analysis

5.3.1. UV-DRS studies

The optical property and the band gap value of the synthesized ferrite nanoparticles were studied and estimated respectively with the help of diffused reflectance UV–visible spectroscopy. The reflectance spectrum was recorded and it is converted to absorption values using Kubelka-Munk (KM) relation as follows.

$$F(R) = \frac{1 - R^2}{2R} \quad (4)$$

The absorption spectrum ranges from 200 to 800 nm for all cobalt ferrite samples were shown in Fig. 2a. It is noted that pure CoFe_2O_4 sample has a broad absorption range i.e. from $\sim 270\text{ nm} - 750\text{ nm}$, and with an increase in Zn content the absorption edge gets shifted towards lower wavelength range ($\sim 750\text{--}600\text{ nm}$). This type of absorption was observed for cobalt ferrites due to narrow bandgap and similar results were reported previously by Tatarchuk et al., Zeng et al., and Singh et al. [40,41, and 38]. The bandgap energy was calculated using Tauc's relation given in equation (4), and it is a graph plotting between $(\alpha h\nu)^2$ and photon energy ($h\nu$) as shown in Fig. 2b.

$$\alpha h\nu = A(h\nu - E_g)^{1/2} \quad (5)$$

where, E_g , ν , A , h , and α are the optical band gap, light frequency, the proportionality constant, Plank's constant, and absorption coefficient respectively.

In general, the band gap value is estimated from the intercept acquire by extrapolating the linear portion of the graph and the optical band gap value of the synthesized particle is found to be 1.85 eV, 1.99 eV, 2.08 eV and 2.28 eV for CFO, ZCF1, ZCF2, and ZCF3 respectively. These obtained values are quiet agree with the results reported by Fan et al. [42]. There was a significant increase in bandgap was observed with an increase in Zn^{2+} content into the CoFe_2O_4 lattice. This may be due to the formation of sub-bandgap and defects in the energy level [43,38]. Eventually, the decrease in crystallite size indicates a very weak quantum size effect and this also one of the reasons for a small increase in the optical bandgap energy [44]. According to the obtained bandgap values thus these materials are active in visible regions.

5.3.2. Photoluminescence studies (PL)

Photoluminescence studies of prepared materials were carried out at room temperature with an excitation wavelength of 320 nm. PL study was used, to experience the recombination factors and to get the details of sub-bandgap defect states and surface defects of the prepared samples [45]. The fluorescence spectrum for all prepared samples, recorded in the wavelength ranges from 350 to 550 nm is shown in Fig. 2c. The near band emission (NBE) observed at 369 nm for all samples are because of the inherent transition of excitons between conduction and valence band [46]. The emission band observed around 452 nm in the violet region is maybe owing to the radiating defects associate with the traps in interfaces that occur at the grain boundaries [47,48]. Another band related to green emission at 512 nm was observed is due to the oxygen vacancies defect in the crystal [49]. Similar emission spectrums for CoFe_2O_4 NPs were observed by Jansi Rani et al. [50]. The intensity of all peaks reduced with the increase in Zn^{2+} content may be due to

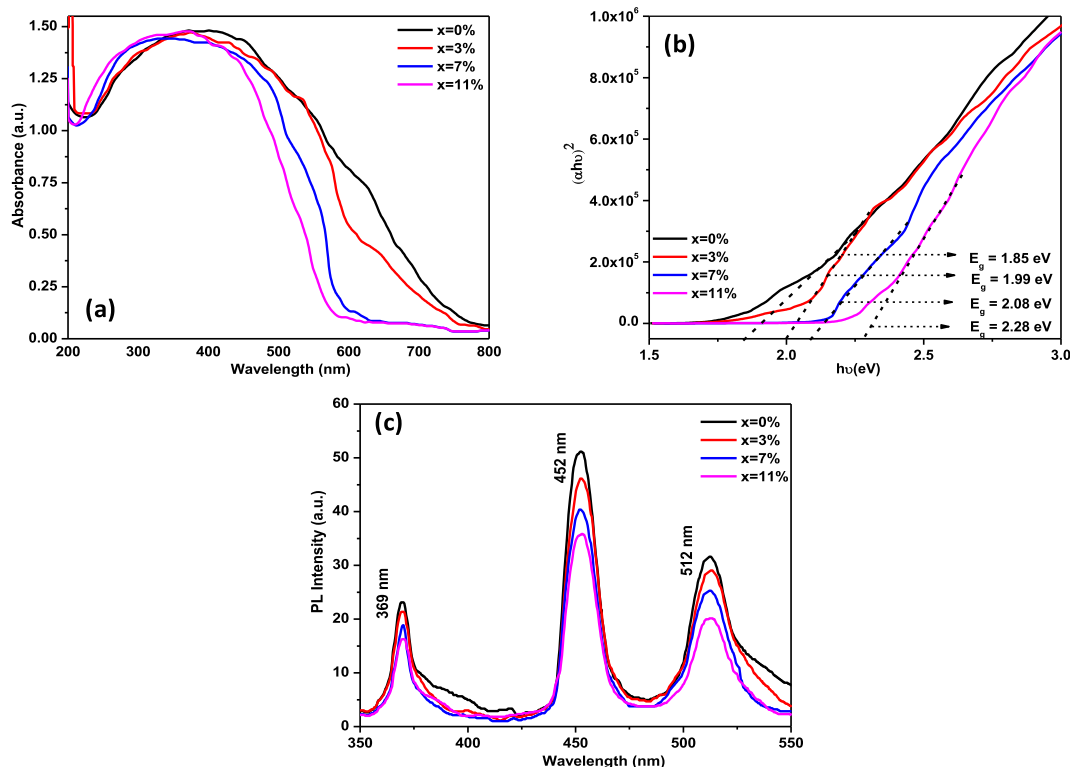


Fig. 2. (a) The UV-DRS absorption spectrum of CoFe_2O_4 and Zn-doped CoFe_2O_4 NPs, (b) The Tauc's plot of CoFe_2O_4 and Zn-doped CoFe_2O_4 NPs and (c) The PL spectrum of CoFe_2O_4 and Zn-doped CoFe_2O_4 NPs.

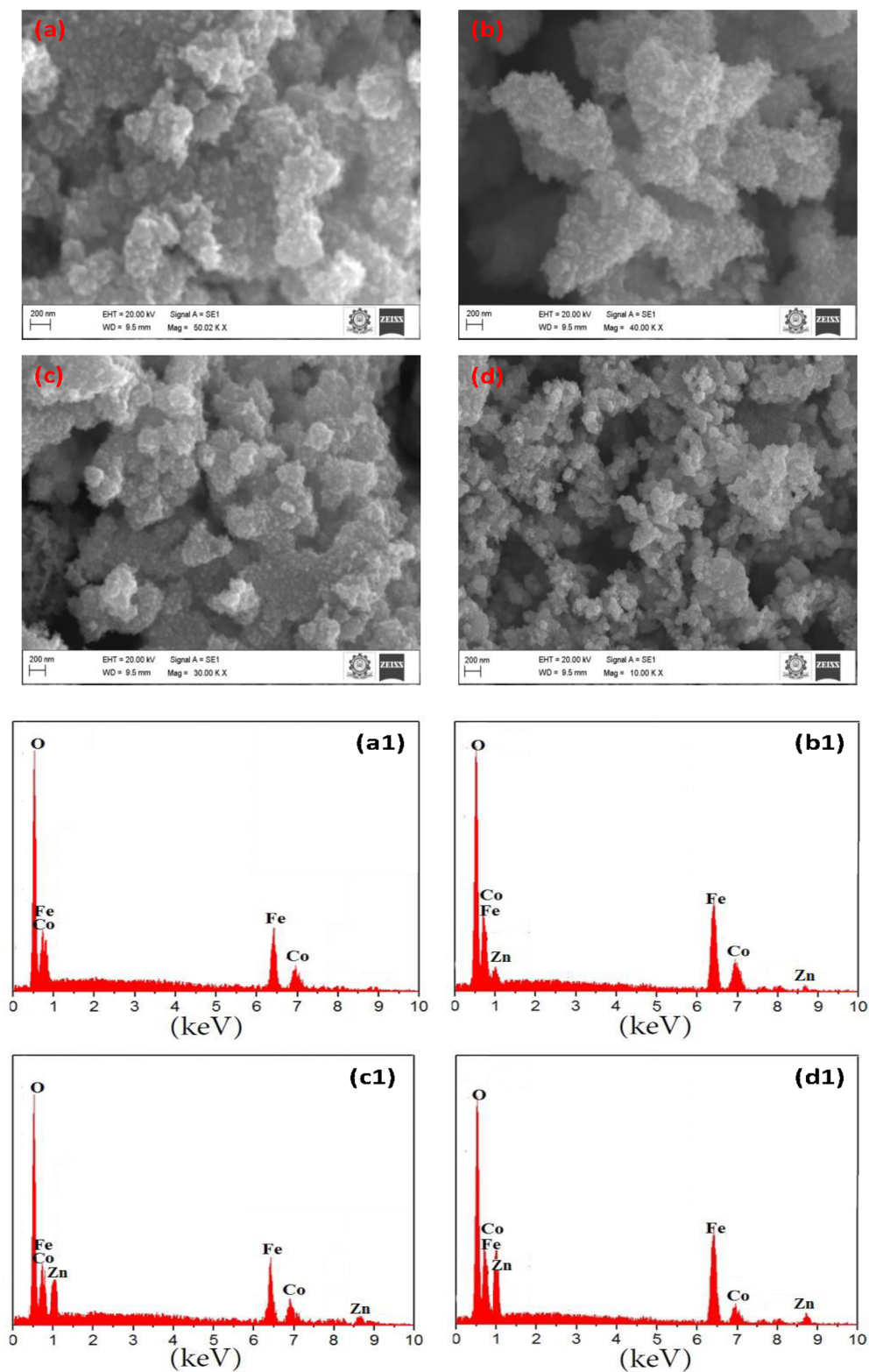


Fig. 3. (a, b, c, d) SEM images and (a1, b1, c1, d1) is EDAX spectrum of CFO, ZCF1, ZCF2, and ZCF3 respectively.

the increase in band gap values which inhibits the rate of electron-hole pair recombination. Also the deep level emission confirms oxygen defect exists in the prepared material which leads to more number of active sites on the surface of the sample thus helps to enhance the photocatalytic behavior.

5.4. SEM and EDAX analysis

The surface morphology of as-prepared samples CFO, ZCF1, ZCF2, and ZCF3 was shown in Fig. 3 (a, b, c, d) respectively. There are no certain shapes are found and agglomerated structure was obtained for pure sample (CFO) and gradually the incorporation of Zn^{2+} ions will

improve the crystallinity of the material is evident from Fig. 3d, the image of ZCF3 sample exhibits some slight spherical morphology. This low crystallinity is because of fast precipitation of the material leads to rapid crystallization and irregular cluster formations. Also all the samples show some rough surface morphology which helps in adsorption of dye molecules during photocatalytic reactions. The elemental composition of the prepared samples CFO, ZCF1, ZCF2, and ZCF3 was shown in Fig. 3 (a1, b1, c1, d1) respectively using EDAX analysis.

5.5. Photocatalytic studies

The photocatalytic experiments with all the synthesized nano photocatalyst were done under direct sunlight at noontime i.e. from 12 to 2 pm on a perfect sunny day. RhB, MB and CV dyes were taken in separate beakers and then the photocatalyst along with H₂O₂ was added under vigorous stirring for achieving complete dispersion of the NPs, also kept in dark for 1 h to attain adsorption/desorption equilibrium. The aliquots of the dye samples were collected every 15 min and subjected to UV-Visible spectroscopy to study the quantity of dye degradation. In general, the photodegradation process occurs by the superoxide anions ($\bullet\text{O}_2^-$) and hydroxyl ($\bullet\text{OH}$) radicals and these are produced when the light hits the semiconductor metal oxides. The light photons excited the electron from the valence band to conduction band and thus the holes are created in the valence band. Then the e^- react with oxygen produces superoxide anions and holes react with water produces hydroxyl radicals. The graph between reduction in initial concentration (C/C_0) and irradiation time for all the dyes was shown in Fig. 4(a, b, c). The maximum degradation percentage was achieved to be 97%, 83% and 91% for MB, RhB, and CV respectively with ZCF3 sample, whereas 41%, 39%, and 49% are obtained with CFO sample for respective dyes MB, RhB, and CV after 90 min of continuous irradiation. The experiment was also done bare synthesized photocatalyst but there is no noticeable change in concentration of dye molecules was observed. This may be because of the faster recombination rate of photo-generated e^-/h^+ pairs in the metal oxides due to its smaller band gap

values. The incorporation of H₂O₂ into the dye solution has drastically increased the degradation performance because hydrogen peroxide acts as a sacrificial electron acceptor and in turn produces sufficient hydroxyl radicals. Moreover, it is observed that for all the dyes, the degradation percentage gradually increased with an increase in Zn content. This is because of the slight increase in band gap which results in slower the recombination rate of electron and holes and is evident from PL studies. Also the surface defects, oxygen vacancies may help to boost up the reduction and oxidation of organic pollutants. An essential photodegradation was attained for the ZCF3 sample due to sufficient delay in the recombination of split up e^-/h^+ pairs; hence the charge carriers are made easily available for the oxidation of dye molecules in the solution. In addition, the crystallite size is smaller for the ZCF3 sample when compared to other samples, so the number of active sites becomes more on the surface of the sample thus will help to enhance photocatalytic behavior. This is also one of the reasons for the maximum efficiency of ZCF3 sample.

The reaction kinetics of CFO, ZCF1, ZCF2, and ZCF3 NPs in the degradation performance of MB, RhB and CV were quantitatively calculated and fitted using the equation (6) called Langmuir-Hinshelwood model. This model narrates the rate constant of the reaction for the photodegradation of dye molecules and is shown in Fig. 5(a, b, c) which gives the chemical kinetics and fits with the pseudo-first-order kinetic model [23]. The rate constant gives information about the approximate number of dye molecules dissociates per second during the photodegradation process.

$$\ln\left(\frac{C}{C_0}\right) = kt \quad (6)$$

where C_0 is the initial concentration of dye solution, C is the change in concentration of dye solution with respect to time, and k is the first-order rate constant. The rate constant value is obtained from the slope by drawing a linear fit for the graph between $\ln(C/C_0)$ and irradiation time. The obtained rate constant values with CFO, ZCF1, ZCF2, and ZCF3 NPs for degradation of MB, RhB and CV dyes are tabulated in

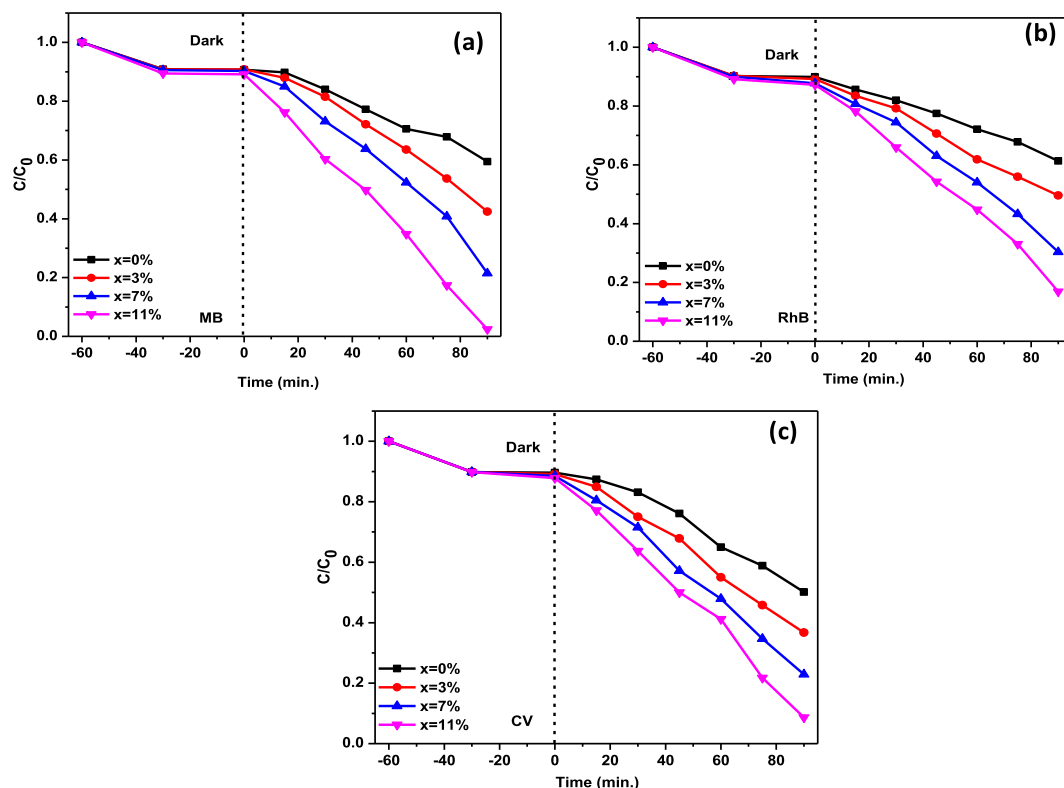


Fig. 4. (a, b & c) Time vs concentration of MB, RhB and CV dye with CFO, ZCF1, ZCF2, and ZCF3,

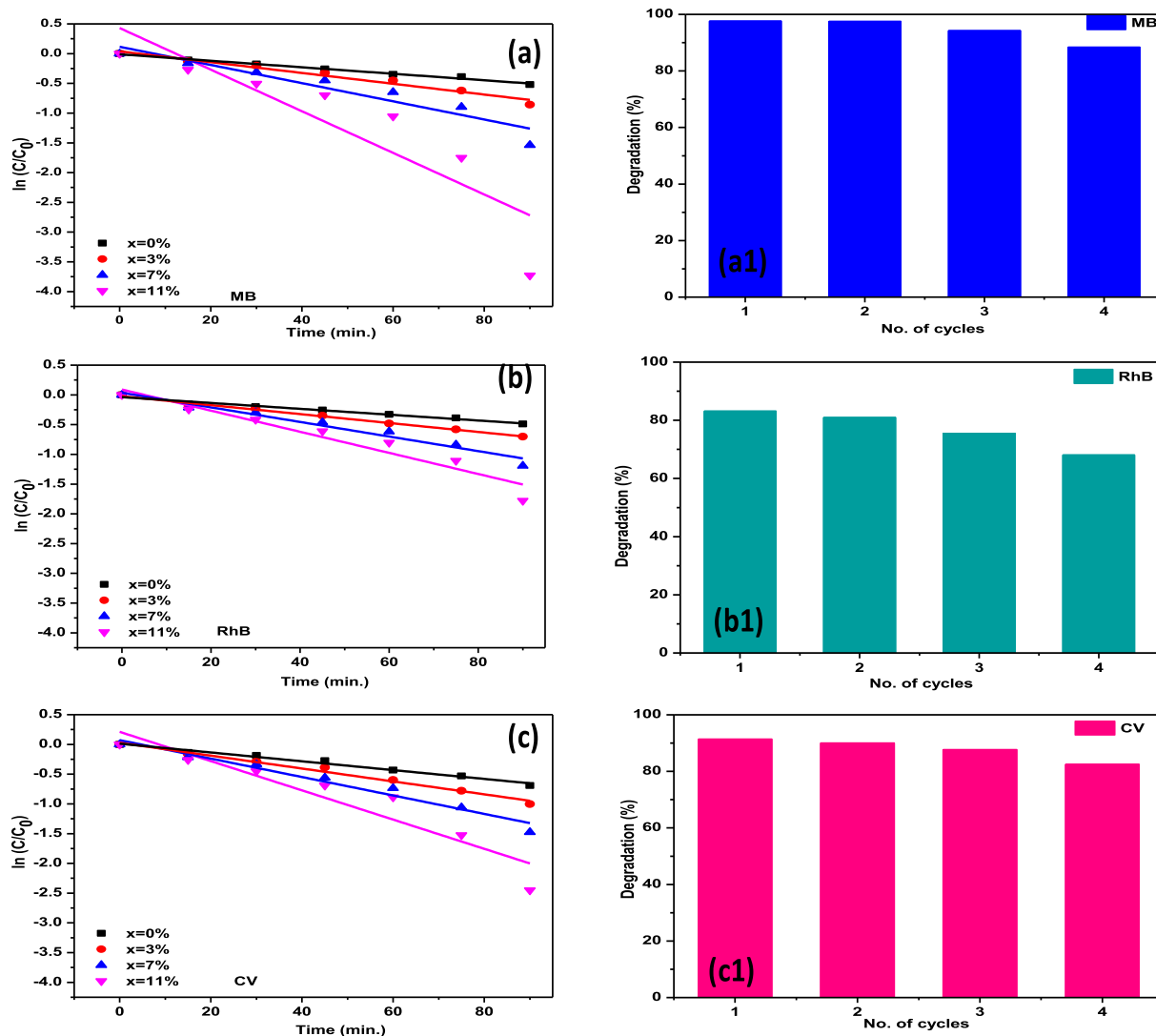


Fig. 5. (a, b & c) Time vs. Rate constant for MB, RhB and CV dye with CFO, ZCF1, ZCF2, and ZCF3, & (a1, b1, c1) recycle ability of ZCF3 sample with MB, RhB and CV dyes.

Table 2

Comparison table of CoFe_2O_4 and Zn-doped CoFe_2O_4 NPs in dye degradation mechanism.

Dye	Samples	Rate constant (k) (s^{-1})	(R^2) value	Degradation %
Methylene Blue	CFO	5.46×10^{-3}	0.98827	41
	ZCF1	9.07×10^{-3}	0.96716	57
	ZCF2	15.28×10^{-3}	0.88851	78
	ZCF3	34.97×10^{-3}	0.75068	97
Rhodamine B	CFO	4.91×10^{-3}	0.96932	39
	ZCF1	7.50×10^{-3}	0.98996	50
	ZCF2	12.25×10^{-3}	0.95705	69
	ZCF3	17.74×10^{-3}	0.91823	83
Crystal Violet	CFO	7.41×10^{-3}	0.97992	49
	ZCF1	10.83×10^{-3}	0.98334	63
	ZCF2	15.84×10^{-3}	0.95802	77
	ZCF3	24.57×10^{-3}	0.87145	91

Table 2. In order to investigate the stability and reusability of the sample ZCF3, the sample was collected by centrifuging the dye solution after degradation and dried in a hot air oven. The procedure was repeated for four cycles and the bar chart represents the reusable ability is shown in Fig. 5 (a1, b1, c1). From the observed results it is clear that the synthesized material has good withstanding ability up to three cycles and shows a slight decrease in efficiency in the fourth cycle. This may

because the surface adsorbed dye molecule will reduce the light-absorbing quality of the material and also damage the material.

6. Conclusion

The cobalt ferrite and zinc doped cobalt ferrite NPs were prepared and analyzed using various characterization techniques for confirming the crystal structure, optical properties like band gap, and identification crystal defects, elemental composition, and functional groups that present in the synthesized materials. Further, the photocatalytic activity of as-prepared material was analyzed using the model pollutants MB, RhB and CV dyes. The high concentration Zn^{2+} doped sample (ZCF3) shows an attractive result among the other samples. Therefore, the substitution of Zn^{2+} cations in the CoFe_2O_4 lattices will highly enhance the photocatalytic activity of CoFe_2O_4 NPs due to the variation in the band gaps and the crystallite size effect. Besides these, the photocatalytic performance was carried out under direct sunlight without any experimental setup confirms that the prepared material was more efficient, eco-friendly and cost-effective for the remediation of wastewater treatment. In addition, the stability check of the sample will add further qualification i.e. durability as well as attractiveness for the prepared material.

Declaration of Competing Interest

The authors declared that there is no conflict of interest.

References

- [1] S. Yang, C. Sun, X. Li, Z. Gong, X. Quan, *J. Hazard. Mater.* 175 (1–3) (2010) 258–266.
- [2] A. Bianco Prevot, C. Baiocchi, M.C. Brussino, E. Pramauro, P. Savarino, V. Augugliaro, L. Palmisano, *Environ. Sci. Technol.* 35 (5) (2001) 971–976.
- [3] S.U. Khan, M. Al-Shahry, W.B. Ingler, *Science* 297 (5590) (2002) 2243–2245.
- [4] S. Song, J. Tu, Z. He, F. Hong, W. Liu, J. Chen, *Appl. Catal. A* 378 (2) (2010) 169–174.
- [5] R. Wang, D. Xu, J. Liu, K. Li, H. Wang, Preparation and photocatalytic properties of CdS/La2Ti2O7 nanocomposites under visible light, *Chem. Eng. J.* 168 (1) (2011) 455–460.
- [6] H.W. Choi, E.J. Kim, S.H. Hahn, *Chem. Eng. J.* 161 (1–2) (2010) 285–288.
- [7] H. Park, W. Choi, *J. Photochem. Photobiol., A* 159 (3) (2003) 241–247.
- [8] J.Y. Patil, D.Y. Nadargi, J.L. Gurav, I.S. Mulla, S.S. Suryavanshi, *Mater. Lett.* 124 (2014) 144–147.
- [9] L. Satyanarayana, C.G. Reddy, S.V. Manorama, V.J. Rao, *Sens. Actuators, B* 46 (1) (1998) 1–7.
- [10] N.N. Gedam, P.R. Padole, S.K. Rithe, G.N. Chaudhari, *J. Sol-Gel Sci. Technol.* 50 (3) (2009) 296–300.
- [11] T.Y. Wei, C.H. Chen, H.C. Chien, S.Y. Lu, C.C. Hu, *Adv. Mater.* 22 (3) (2010) 347–351.
- [12] N. Padmanathan, S. Selladurai, *Ionics* 20 (4) (2014) 479–487.
- [13] L. Luo, H. Qiao, K. Chen, Y. Fei, Q. Wei, *Electrochimica Acta* 177 (2015) 283–289.
- [14] S. Åsbrink, A. Waškowska, J.S. Olsen, L. Gerward, *Physical Review B* 57 (9) (1998) 4972.
- [15] P.N. Lisboa-Filho, C. Vila, M.S. Góes, C. Morilla-Santos, L. Gama, E. Longo, C.O. Paiva-Santos, *Mater. Chem. Phys.* 85 (2–3) (2004) 377–382.
- [16] Y. Chen, L. Hu, M. Wang, Y. Min, Y. Zhang, *Colloids Surf., A* 336 (1–3) (2009) 64–68.
- [17] S.A. Hassanzadeh-Tabrizi, R. Pournajaf, A. Moradi-Paradonbeh, S. Sadeghinejad, *Ceram. Int.* 42 (12) (2016) 14121–14125.
- [18] T. Larbi, K. Doll, M. Amlouk, *Spectrochimica Acta Part A: Molecular and Biomolecular Spectroscopy* 216 (2019) 117–124.
- [19] Y.Y. Jiang, J.W. Zhang, Z.Q. Hu, J.X. Liu, *Applied Mechanics and Materials* 455 (2013) 99–105.
- [20] S. Joshi, M. Kumar, S. Chhoker, A. Kumar, M. Singh, *J. Magn. Magn. Mater.* 426 (2017) 252–263.
- [21] M. Vadivel, R.R. Babu, K. Ramamurthi, M. Arivanandhan, *Ceram. Int.* 42 (16) (2016) 19320–19328.
- [22] A. Franco Jr, H.V.S. Pessonni, F.O. Neto, J. Alloy. *Compd.* 680 (2016) 198–205.
- [23] A.I. Borhan, P. Samoila, V. Hulea, A.R. Iordan, M.N. Palamaru, *J. Photochem. Photobiol. Chem.* 279 (2014) 17–23.
- [24] M. Rahimi-Nasrabadi, M. Behpour, A. Sobhani-Nasab, M.R. Jeddy, *J. Mater. Sci.: Mater. Electron.* 27 (11) (2016) 11691–11697.
- [25] R. Sharma, S. Singhal, *J. Chem. Technol. Biotechnol.* 90 (5) (2015) 955–962.
- [26] S.K. Jesudoss, J.J. Vijaya, L.J. Kennedy, P.I. Rajan, H.A. Al-Lohedan, R.J. Ramalingam, M. Bououdina, *J. Photochem. Photobiol. B Biol.* 165 (2016) 121–132.
- [27] A. Samavati, A.F. Ismail, *Particuology* 30 (2017) 158.
- [28] J. Ahmed, S.M. Alshehri, A.N. Alhabarah, T. Ahmad, *Chem Electro Chem* 4 (2017) 2952.
- [29] D.H. Kim, D.E. Nikles, D.T. Jhonson, C.S. Brazel, *J. Magn. Magn. Mater.* 320 (2008) 2390.
- [30] Paulsen J.A., Ring A. P, Lo C.C.H., Snyder J.E., Jiles D.C. (2005), *J. Appl. Phys.* 97, 044502.
- [31] D. Erdem, N.S. Bingham, F.J. Heiligtag, N. Pilet, P. Warnicke, L.J. Heyderman, M. Niederberger, *Adv. Funct. Mater.* 26 (2016) 1954.
- [32] K. Kombariah, J.J. Vijaya, J.L. Kennedy, *Mater. Chem. Phys.* 204 (2018) 410–419.
- [33] M.P. Pileni, *Adv. Funct. Mater.* 11 (2001) 323.
- [34] Z. Li, J. Ai, M. Ge, *J. Environ. Chem. Eng.* 5 (2017) 1394–1403.
- [35] M. Sundararajan, L.J. Kennedy, P. Nithya, J.J. Vijaya, M. Bououdina, *J. Phys. Chem. Solid.* 108 (2017) 61–75.
- [36] A. Kalam, A.G. Al-Sehemi, M. Assiri, G. Du, T. Ahmad, I. Ahmad, M. Pannipara, *Results Phys.* 8 (2018) 1046–1053.
- [37] L. Gan, S. Shang, C.W.M. Yuen, S.X. Jiang, E. Hu, *Appl. Surf. Sci.* 351 (2015) 140–147.
- [38] C. Singh, A. Goyal, S. Singhal, *Nanoscale* 6 (14) (2014) 7959–7970.
- [39] A.M. El Sayed, *Ceram. Int.* 28 (2002) 363–367.
- [40] T. Tatarchuk, M. Bououdina, W. Macyk, O. Shyichuk, N. Paliychuk, I. Yaremiy, M. Pacia, *Nanoscale Research Letters* 12 (1) (2017).
- [41] Y. Zeng, N. Guo, Y. Song, Y. Zhao, H. Li, X. Xu, H. Yu, *J. Colloid Interface Sci.* 514 (2018) 664–674.
- [42] Fan, G., Tong, J., & Li, F. (2012), 51(42), 13639–13647.
- [43] C. Singh, S. Jauhar, V. Kumar, J. Singh, S. Singhal, *Mater. Chem. Phys.* 156 (2015) 188–197.
- [44] N. Kislova, S.S. Srinivasan, Y. Emirov, E.K. Stefanakos, *Mater. Sci. Eng., B* 153 (2008) 70–77.
- [45] R. Bhargava, P.K. Sharma, R.K. Dutta, S. Kumar, A.C. Pandey, N. Kumar, *Mater. Chem. Phys.* 120 (2–3) (2010) 393–398.
- [46] A. Ray, M. Roy, J. Ghosh, A. Ramos-Ramon, S. Saha, U. Pal, S.K. Bhattacharya, S. Das, *Appl. Surf. Sci.* 463 (2019) 513–525.
- [47] C.H. Zang, D.M. Zhang, C.J. Tang, S.J. Fang, Z.J. Zong, Y.X. Yang, Y.S. Zhang, *The Journal of Physical Chemistry C* 113 (43) (2009) 18527–18530.
- [48] L.J. Zhuge, X.M. Wu, Z.F. Wu, X.M. Yang, X.M. Chen, Q. Chen, *Mater. Chem. Phys.* 120 (2–3) (2010) 480–483.
- [49] A. Manikandan, S.A. Antony, R. Sridhar, S. Ramakrishna, M. Bououdina, *J. Nanosci. Nanotechnology* 15 (7) (2015) 4948–4960.
- [50] B.J. Rani, M. Ravina, B. Saravanakumar, G. Ravi, V. Ganesh, S. Ravichandran, R. Yuvakkumar, *NANO-Structures & Nano-Objects* 14 (2018) 84–91.
- [51] W.B. Carpenter, J.A. Fournier, R. Biswas, G.A. Voth, A. Tokmakoff, *J. Chem. Phys.* 147 (8) (2017) 084503.45.
- [52] M.H. Habibi, H.J. Parhizkar, *Spectrochimica Acta Part A: Molecular and Biomolecular Spectroscopy* 127 (2014) 102–106.